Review article **Open Access**

Genta Masada and Akira Furusawa*

On-chip continuous-variable quantum entanglement

DOI 10.1515/nanoph-2015-0142
Received November 18, 2015; revised February 3, 2016; accepted March 21, 2016

Abstract: Entanglement is an essential feature of quantum theory and the core of the majority of quantum information science and technologies. Quantum computing is one of the most important fruits of quantum entanglement and requires not only a bipartite entangled state but also more complicated multipartite entanglement. In previous experimental works to demonstrate various entanglement-based quantum information processing, light has been extensively used. Experiments utilizing such a complicated state need highly complex optical circuits to propagate optical beams and a high level of spatial interference between different light beams to generate quantum entanglement or to efficiently perform balanced homodyne measurement. Current experiments have been performed in conventional free-space optics with large numbers of optical components and a relatively large-sized optical setup. Therefore, they are limited in stability and scalability. Integrated photonics offer new tools and additional capabilities for manipulating light in quantum information technology. Owing to integrated waveguide circuits, it is possible to stabilize and miniaturize complex optical circuits and achieve high interference of light beams. The integrated circuits have been firstly developed for discrete-variable systems and then applied to continuous-variable systems. In this article, we review the currently developed scheme for generation and verification of continuous-variable quantum entanglement such as Einstein-Podolsky-Rosen beams using a photonic chip where waveguide circuits are integrated. This includes balanced homodyne measurement of a squeezed state of light. As a simple example, we also review an experiment for generating discrete-variable quantum entanglement using integrated waveguide circuits.

Keywords: silica-on-silicon chip; waveguide interferometer; EPR beams; squeezed light; balanced homodyne measurement.

1 Introduction

The key part of quantum information processing is controlling a quantum state. Quantum teleportation is a scheme to transfer a quantum state utilizing not only the classical channel but also quantum entanglement and an essential protocol for realizing quantum computing [1]. In previous experimental studies, light has been extensively used to demonstrate quantum teleportation [2, 3] and entanglement-based quantum computing [4, 5].

There are two natural ways to encode information in the quantum domain. One is to use two discrete levels of a single photon (e.g. two orthogonal polarizations or two optical paths of a single photon) that describe discrete variables (DVs). The other is to use a quadrature phase amplitude of an electromagnetic field (e.g. a coherent light or squeezed light) that describes continuous variables (CVs). In accordance with the two methods of encoding quantum information, there are mainly two types of quantum entanglement. One is DV entanglement, typically a pair of entangled photons [6], or NOON states [7]. The other is CV entanglement such as Einstein-Podolsky-Rosen (EPR) [8] beams, which correspond to two-mode squeezed light in the case with infinite squeezing. In this article, however, we represent EPR beams for both cases with infinite and finite squeezing.

The DV systems benefit from high-fidelity operations like a digital information technology, but are limited by the imperfect generation and detection of single photons. In contrast, CV schemes can achieve a deterministic and unconditional operation, while the fidelities are not so high for the majority of quantum protocols. A newly developed hybridization approach can overcome these problems by combining the benefits of DVs and CVs in a

***Corresponding author: Akira Furusawa,** The University of Tokyo, Hongo, Bunkyo-ku, Tokyo, Japan, e-mail: akiraf@ap.t.u-tokyo.ac.jp
Genta Masada: The University of Tokyo, Hongo, Bunkyo-ku, Tokyo, Japan; and Tamagawa University, Tamagawagakuen, Machida, Tokyo, Japan

Edited by Volker Sorger

single system [9]. One of the significant experiments is hybrid quantum teleportation of photonic quantum bits using CV quantum teleportation schemes [10]. In this experiment, quantum information is encoded on a single-photon; EPR beams are used as a quantum entanglement resource; and balanced homodyne measurement is applied to make deterministic Bell-state measurements.

Another important approach in quantum information processing is measurement-based one-way quantum computation with multi-partite quantum entanglement such as cluster states [11–14]. CV systems have an advantage over DVs, as CV cluster states can be unconditionally prepared with squeezed light sources and beam splitters [15]. In addition, balanced homodyne detection is available as a deterministic measurement. CV cluster states with four optical modes are generated and applied to unconditional one-way quantum computation in the frequency domain [16]. An ultra-large-scale CV cluster state containing >10,000 modes is also generated by using a time-domain multiplexing method [17]. A current theoretical work shows that fault-tolerant quantum computing is possible with CV cluster states obtained by highly squeezed light source [18] and Gottesman-Kitaev-Preskill encoding [19] with cat states [20].

These important proof-of-principle experiments have been performed in conventional free-space optics in which photons or light beams propagate through complex optical circuits consisting of a lot of mirrors, beam splitters, and lenses. Such a scheme has limited stability due to the relatively large-sized optical setup. Practical applications of quantum information technology require an integrated waveguide circuit in which photons or light beams are guided, manipulated, and interfered. Integrated waveguide circuits have been successfully developed for DV applications by O'Brien's group in Bristol [21, 22], and they have demonstrated high-fidelity and reliable operations [23]. More recently, integrated waveguide circuits are applied for CV applications [24]. Generation and verification of EPR-entangled beams, including balanced homodyne measurement, is demonstrated by using an integrated waveguide circuit. A benefit of this optical integration is stabilization and miniaturization of quantum circuits and attainment of a high degree of spatial mode matching, which is essential for both classical and quantum interference. Fiber optics is also important for guiding light beams and stabilizing an optical system, and then applied for various CV applications [25–29].

In this article, we mainly review the current development in integrated photonic implementation of EPR beams and balanced homodyne measurement, which are important for CV as well as hybrid quantum information processing. In Section 2, we briefly review an integrated waveguide circuit and the generation of photon-entangled states as an example of DV entanglement to better understand CV experiments in the following sections. Section 3 shows balanced homodyne detection of a CV quantum state, such as squeezed states of light. Section 4 shows generation and verification of EPR beams. Finally, we conclude this review article in Section 5.

2 DV entanglement in a photonic chip

In this section, we review the currently developed quantum optics experiments that generate and characterize DV entanglement using a photonic chip where waveguide Mach-Zender interferometers are integrated [21, 22]. As a simple example, we focus on the states described as $1/\sqrt{2}(|1\rangle|0\rangle\pm|0\rangle|1\rangle)$ and $1/\sqrt{2}(|2\rangle|0\rangle-|0\rangle|2\rangle)$. They correspond to NOON states of N=1 and 2, respectively [7]. The latter state is known as the Hong-Ou-Mandel (HOM) state [30]. The entangled HOM state is an important resource for phase-estimation technology based on quantum metrology [31] and precise processing technology based on quantum optical lithography [32]. Two-photon interference is also an essential interaction for the Knill-Laflamme-Milburn (KLM) scheme, which yields a fully scalable quantum computer [33].

2.1 Construction of integrated waveguide circuits

Figure 1A [22] presents a schematic of a waveguide circuit integrated in a silica-on-silicon chip. The circuit is composed of a pair of directional couplers and a resistive heater (R) lithographically defined on top of one waveguide arm. These elements construct a waveguide interferometer. A precise design and fabrication of the directional coupler enables mixing two light beams with high mode-matching efficiency and an exact beam-splitting ratio [21]. Inset B shows the cross section view of the chip. The waveguide circuit is fabricated on silicon wafer (I). The waveguide core (III) has 3.5 μm squared dimensions and is surrounded by lower refractive index cladding (II, IV). The spacing between each waveguide core is 250 μm. Optical wave is confined in the core region and propagates through the waveguide. Inset C shows the simulation result of the intensity distribution of the guided optical wave and a feature of almost single mode. By tuning the electrical voltage applied for resistive heater (R) on contact with pads p_1 and p_2, it is possible to raise

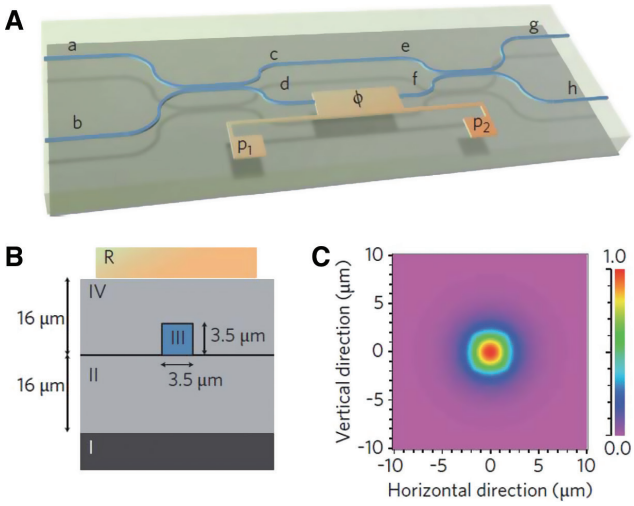

Figure 1: (A) Schematic of a waveguide interferometer. (B) Cross-section view of the waveguide structure. (C) A simulation result of the optical mode in the waveguide [22].

the temperature of one waveguide arm and then control the phase difference ϕ between two arms. So, the resistive heater is used as a voltage-controlled phase shifter. Owing to this feature, the waveguide interferometer can work as a continuously variable beam splitter. More details will be described in Section 3.3.

2.2 Generation of photon-entangled states

Figure 2A and B [22] show the experimental result of one-photon and two-photon interference using the waveguide interferometer as shown in Figure 1A. A single-photon or indistinguishable two single-photon state is generated outside the chip by a spontaneous-parametric-down conversion process with a type-I non-linear optical crystal and a pulsed laser light source. In Figure 2A, a single photon is introduced from input port a. The one-photon count rates are measured by two single-photon counting modules at output ports g and h, by varying a phase of the waveguide interferometer. The observed sinusoidal pattern arises from one-photon interference. The output states correspond to one-photon entangled states $1/\sqrt{2}(|1\rangle|0\rangle\pm|0\rangle|1\rangle)$ at the phase of $\pm\pi/2$. In Figure 2B, the two-photon coincidental count rate is measured at output ports g and h by introducing two single-photon states from a and b. The significant sinusoidal fringe arises from two-photon interference as two photons are indistinguishable and arrive simultaneously at the waveguide interferometer. The output state is the HOM state, $1/\sqrt{2}(|2\rangle|0\rangle-|0\rangle|2\rangle)$ at the phase of $-\pi/2$.

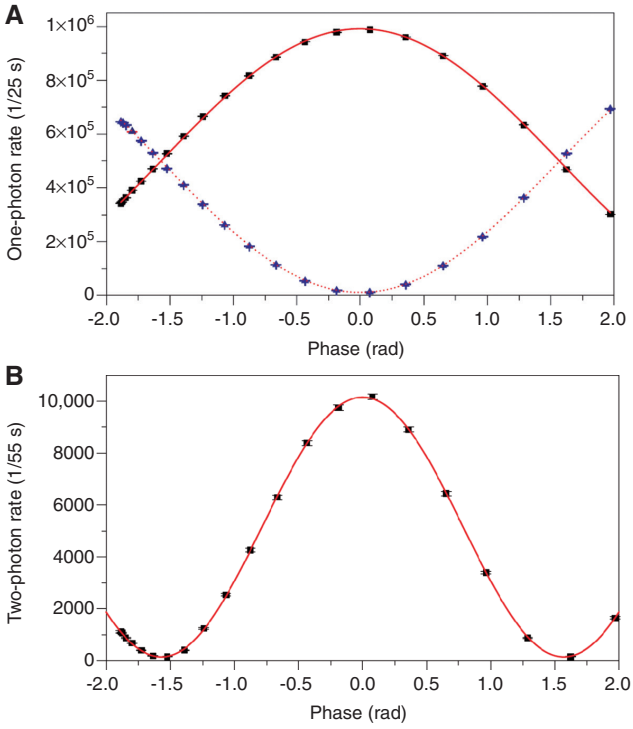

Figure 2: (A) One-photon count rates observed at two output ports g and h when inputting the single-photon from input port a of the waveguide interferometer. (B) Two-photon coincident count rates between outputs at g and h when inputting the two single-photons from input ports a and b. Both experiments are conducted by varying a phase ϕ, which is controlled by a voltage applied to the phase shifter [22].

Figure 3 [22] shows the visibility of the HOM dip at certain phases obtained by scanning a relative delay time between incident two single-photons outside the photonic chip as shown in the insets. At the phase of $-\pi/2$, the maximum HOM dip is obtained.

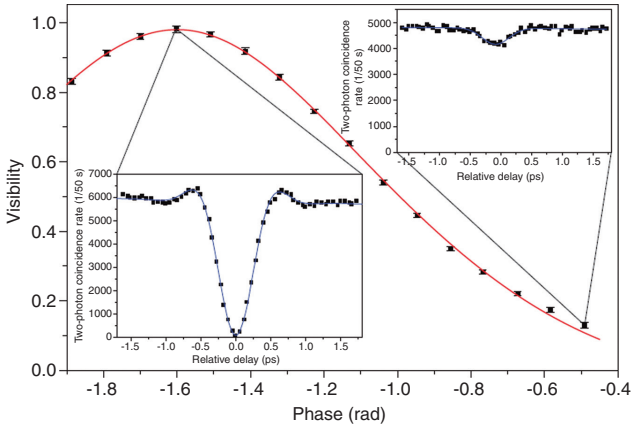

Figure 3: Visibility of the HOM interference obtained by using the integrated waveguide interferometer that is controlled as a variable beam splitter [22].

The experiments reviewed already are demonstrated with only one waveguide interferometer. However, in a recent work, a reprogrammable optical circuit in a single photonic chip where many waveguide interferometers and phase shifters are integrated is applied to the realization of universal linear optics [34, 35]. The universal linear optical component is a required element for constructing a fully scalable quantum computer based on KLM scheme together with single photon detectors and single photon sources [33]. The above experiments use a single-photon resource generated outside a chip. However, current experimental works demonstrate on-chip direct generation of DV entanglement by using a directional coupler, waveguide arrays consisting of a non-linear optical crystal [36, 37], and integrated waveguide circuits with a silicon-on-insulator photonic platform, which utilize spontaneous four-wave mixing process [38].

3 Demonstration of balanced homodyne measurement for squeezed light in a photonic chip

3.1 Balanced homodyne measurement using a waveguide beam splitter

We review the balanced homodyne measurement of squeezed light [24] by using a waveguide beam splitter that is the same as Figure 1A. Balanced homodyne measurement is also applied to the verification of quantum entanglement in EPR beams in Section 4. Historically, Yuen and Chan theoretically developed balanced homodyne measurement as a method for measuring quadrature squeezing in 1983 [39]. Since then, it has become the standard method to measure squeezed light and has been applied to many quantum optics experiments. In order to perform balanced homodyne measurement, it is required to combine squeezed light and local oscillator (LO), which is in a coherent state with high intensity using an exact 50/50 beam splitter. Two output beams from the beam splitter are detected by two photodiodes of a balanced homodyne detector. A subtraction signal of the photocurrents is detected and amplified by low-noise electrical circuits. In this balancing process, an excess classical noise of the local oscillator is cancelled.

In free-space optics, however, a dielectric multilayer beam splitter is used. The accuracy of the beam-splitting ratio depends on the process of optical coating. There is usually a margin of error with a few percent. So, in the actual experiment, fine tuning of beam-splitting ratio is performed by tilting a beam splitter angle. However, by using a waveguide beam splitter, the final tuning of beam-splitting ratio can be easily achieved by adjusting the electrical currents of heaters. This is one of the biggest advantages of a waveguide beam splitter.

For efficient balanced homodyne measurement, it is necessary to combine squeezed light and local oscillator beams with a high level of spatial mode matching. In free-space optics, high mode-matching efficiency is obtained by a precise optical alignment by using optical lenses for mode shaping or adjusting optical path length. By using a waveguide beam splitter, a high level of mode matching can be easily obtained, as the spatial mode is automatically formed by the waveguide mode, if once the optical beams are injected into waveguides. This is another advantage of a waveguide beam splitter.

In waveguide optics, stray light arising from insufficient coupling to waveguides, waveguide bending losses, and cladding guiding causes a crosstalk between different waveguide modes. Such an unwanted crosstalk is a major limitation factor in quantum optical networks, reducing the fidelities of quantum operations. In quantum optics experiments with CVs, the quantum information is often encoded on side bands of optical fields, which are far from the noise spectrum caused by stray light. Moreover, balanced homodyne measurement can sensitively detect the signal spectrum at side-band modes. So, quantum optics experiments with CVs are suitable for the optical integration. In Sections 3 and 4, all balanced homodyne measurements are performed at the 1.5 MHz side bands of the laser frequency to avoid the harmful effects of stray light.

3.2 Experimental setup

The experimental setup for balanced homodyne measurement is shown in Figure 4. Figure 5 is a picture of a silica-on-silicon chip where a number of waveguide interferometers are integrated in parallel. A continuous-wave Ti:Sapphire laser at 860 nm is used as a light source. Squeezed light SL_1 at 860 nm is generated by subthreshold optical parametric oscillator (OPO_1) outside the chip. The OPO_1 consists of an optical cavity with a bow-tie configuration and a periodically poled potassium titanyl phosphate (PPKTP) crystal as a non-linear optical medium [40, 41]. The optical cavity consists of two spherical mirrors with curvature radius of 50 mm and two flat mirrors. One of the flat mirrors has a partial transmittance of 0.113 at 860 nm and is used as an output coupler. The other three mirrors have high reflectivity at 860 nm. All mirrors have

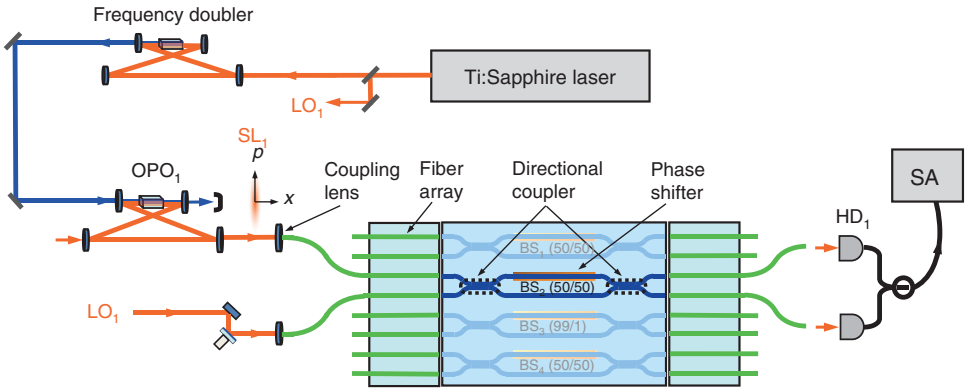

Figure 4: Experimental setup for balanced homodyne measurement of squeezed light in the photonic chip. Beam splitter BS_2 is tuned at a 50/50 beam-splitting ratio. A pair of fiber arrays is used for both entrance and exit facets of the chip to inject and eject beams efficiently. In order to efficiently introduce outer beams to the fibers, aspheric lenses are used for coupling lenses. Continuous-wave squeezed light SL_1 (at 860 nm) is generated by subthreshold optical parametric oscillator (OPO_1) outside the chip. A pump beam at 430 nm for the OPO_1 is generated by an optical frequency doubler. Squeezed light SL_1 is combined with local oscillator LO_1 at beam splitter BS_2 and then detected by homemade balanced homodyne detector HD_1, which has 10 MHz of bandwidth and analyzed by spectrum analyzer SA [24].

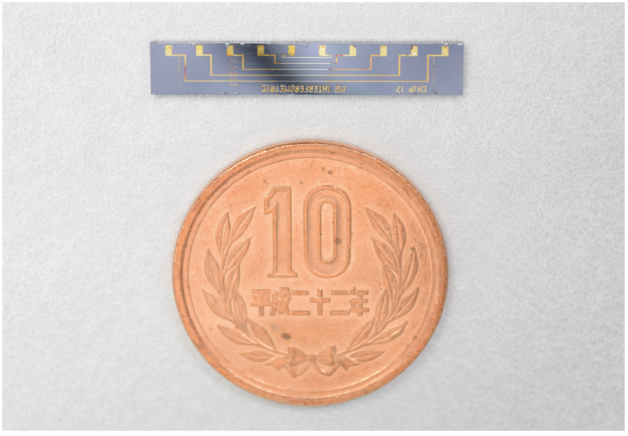

Figure 5: A picture of the photonic chip used in experiments. Waveguide interferometers are integrated in the chip, which has 26 mm length.

high transmissivity at 430 nm. The round-trip length of the cavity is 500 mm. The PPKTP crystal has 10 mm length and 1*1 mm^2 of cross section, and is placed between two spherical mirrors. The crystal temperature is kept at 40°C for achieving a phase matching condition. A pump beam at 430 nm for OPO_1 is generated by an optical frequency doubler, which has the same optical configuration with the OPO_1 but includes a periodically poled MgO-doped lithium niobate crystal [42]. Squeezed light SL_1 is generated by pumping the OPO_1 with the 430 nm beam below an oscillation threshold power. Local oscillator LO_1 is a part of the light source and has the same wavelength with squeezed light SL_1. A weak coherent beam of 860 nm is also introduced into the OPO_1 for the purpose of phase locking. For balanced homodyne measurement, squeezed light SL_1 and local oscillator LO_1 are introduced into the chip and combined at beam splitter BS_2, which is tuned at a 50/50 beam-splitting ratio. Output beams from beam splitter BS_2 are measured by balanced homodyne detector HD_1 outside the chip.

In order to efficiently inject squeezed light SL_1 and local oscillator LO_1 to the waveguides and eject the output beams, a pair of fiber arrays is used for both entrance and exit facets of the chip. On fiber array assembly, single-mode, polarization-maintaining fibers are arranged on a V-grooved Si substrate at an interval of 250 μm. The fiber core diameter is chosen as 5 μm, which is comparable to waveguide core size. The fiber clad diameter is 125 μm. The chip is attached on an aluminum plate that is fixed on a rigid stage. In order to realize a high fiber-to-waveguide coupling efficiency, two fiber arrays are separately mounted on two six-axis positioning stages. One is set at the entrance side and the other is at the exit side of the chip for aligning the position and orientation of fiber arrays with a high degree of accuracy, as shown in Figure 6A. When the optical alignment is performed, views of the interface between the fiber array and chip from a top and side are monitored by using stereomicroscopes, as shown in Figure 6B and C. Firstly, positioning stages are moved in order to align the fiber arrays as close and parallel as possible. Finally, the gaps between fiber arrays and chip are filled with an index matching fluid to eliminate reflection losses. Then, the fiber-to-waveguide coupling efficiency is improved.

All beams, squeezed light SL_1, and local oscillator LO_1 are coupled to the fibers whose end faces are designed as ferrule connector/angled physical contact (FC/APC). To make better fiber coupling efficiency, aspheric lenses with

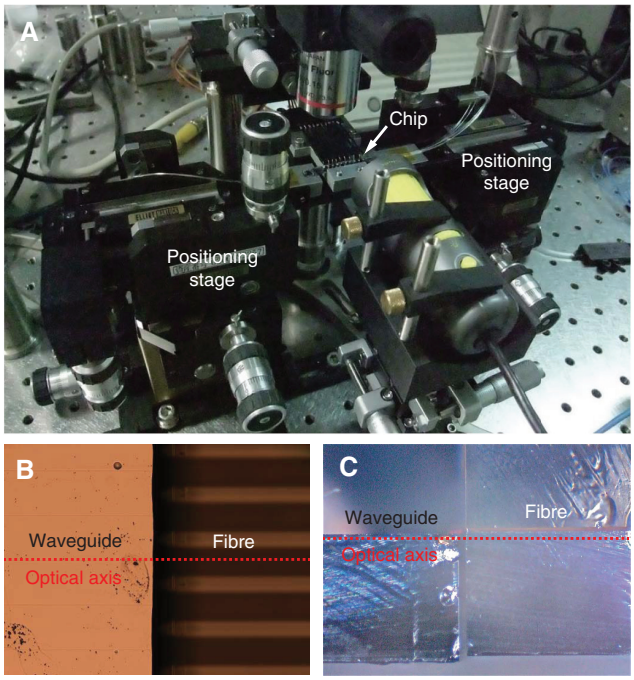

Figure 6: (A) A mechanical setup for the optical alignment. The photonic chip is fixed on a rigid stage and a pair of fiber arrays is mounted on positioning stages for the precise optical alignment. Top view (B) and side view (C) of the interface between the photonic chip and fiber array facet.

focal length of 8 mm and numerical aperture of 0.5 are used. Then, the beam size is focused comparable to the fiber core diameter. An overall coupling efficiency η_c=0.72 is measured by introducing a weak coherent beam into the fiber coupling lens and collecting the output intensity at the fiber exit. The overall coupling efficiency is given as $\eta_c=\eta_f*\eta_w^2$, where η_f is the fiber coupling efficiency and η_w is the fiber-to-waveguide coupling efficiency. η_f is obtained as 0.87 with a direct measurement, and then η_w is estimated as 0.91 on average. The waveguide transmission loss is negligibly small.

3.3 Balance tuning

In order to perform balanced homodyne measurement, it is required to use an exact 50/50 beam splitter and achieve high balance of optical powers at each photodiode of a homodyne detector. In this work, it is especially required to achieve high balance at the 1.5 MHz side band of the laser frequency, as all of the balanced homodyne measurement is performed at this frequency in order to avoid harmful effects from stray light. Figure 7 shows an experimental result of variable beam splitter BS_2. An electric current for the phase shifter of beam splitter BS_2 is supplied through

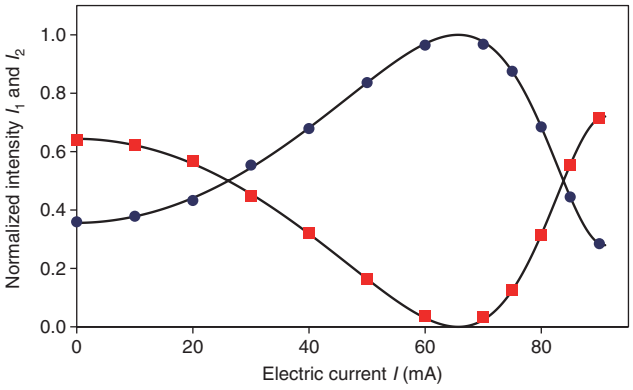

Figure 7: Test result of beam-splitting ratio at various electric currents I for a phase shifter. A weak coherent beam is introduced into a waveguide interferometer and the intensities of two output beams are detected by photodiodes. Blue and red circles represent normalized intensity I_1 and I_2, respectively. Solid lines are fitting results using Eqs. (1), (2), and (3).

metal contact pads p_1 and p_2, as shown in Figure 1A, with a current source. In this experiment, only local oscillator LO_1 is introduced to beam splitter BS_2. The intensities from two-split local oscillator beams are monitored at output fibers with photodiodes separately. The vertical axis shows normalized intensity of output beams I_1 from the lower exit and I_2 from the upper exit of beam splitter BS_2. They correspond to the beam-splitting ratio of the waveguide interferometer at a certain current. Solid lines indicate fitting curves using the following equations:

$$I_1=T_r^2+(1-T_r)^2-2T_r(1-T_r)\cos(\phi), \quad (1)$$

$$I_2=2T_r(1-T_r)+2T_r(1-T_r)\cos(\phi). \quad (2)$$

Both directional couplers are assumed to have the same value of intensity transmissivity T_r. Optical phase ϕ is assumed as a polynomial function of electric current I [18]

$$\phi=\alpha+\beta I^2+\gamma I^3+\delta I^4, \quad (3)$$

where I is varied from 0 to 90 (mA) in this experiment. The parameters are estimated to achieve the best fit for experimental results and found at T_r=0.7644, α=0.6637, β=1.087*10^{-3}, γ=-1.646*10^{-5}, and δ=1.318*10^{-7}.

It is obvious that the beam-splitting ratio of the waveguide interferometer is controlled by electric current I. The waveguide interferometer can therefore work as a variable beam splitter at a certain range, 0.36–1 for output I_1 and 0–0.64 for output I_2. Actually, it is difficult technology to fabricate a directional coupler with just beam-splitting ratio as designed. In balanced homodyne measurement, however, an exact 50/50 beam splitter is required for noise

cancellation. So, the variable beam splitter consisting of a waveguide interferometer is suitable for practical use.

Figure 8 shows an experimental result of precise balance tuning by using beam splitter BS_2. In this experiment, only local oscillator LO_1 is introduced to beam splitter BS_2, divided in two beams, and then observed by homodyne detector HD_1. There are two types of electrical signals analyzed by a spectrum analyzer in Figure 8. Trace (i) shows a signal from one of the photodiodes of homodyne detector HD_1 with measuring one of the divided local oscillator LO_1 beams. A large signal at 1.5 MHz is the amplitude noise created by an electro-optical modulator outside the chip. Another noise at around low frequency is a laser-originated noise. Trace (ii) is a subtraction signal from both photodiodes with measuring both of divided local oscillator LO_1 beams. While measuring trace (ii), the electrical current for the phase shifter of beam splitter BS_2 is firstly kept at around 26 mA, which corresponds to an approximate 50/50 splitting ratio, as shown in Figure 7. Then, the current is finely tuned in order to minimize signals at 1.5 MHz. The final result shows the noise reduction of about -40 dB. The beam splitter BS_2 can provide an almost exact 50/50 splitting ratio and be used for balanced homodyne measurement.

3.4 Result of balanced homodyne measurement of squeezed light

Figure 9 [24] presents a typical result of balanced homodyne measurement of squeezed light SL_1. A pump beam

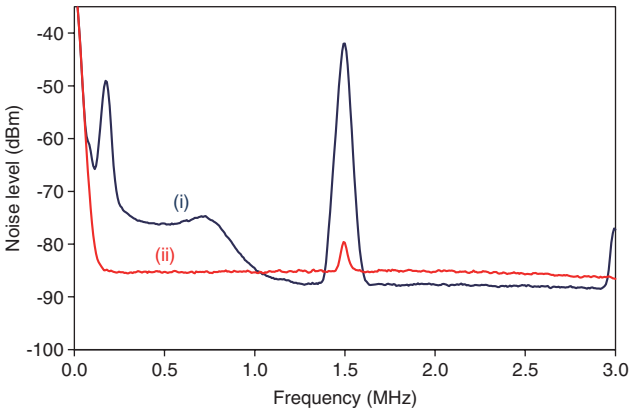

Figure 8: Test result of balance tuning at beam splitter BS_2. A weak coherent beam with a large amplitude noise at 1.5 MHz is introduced into beam splitter BS_2, which is tuned at an exact 50/50 beam splitter. Trace (i) shows a noise spectrum from one of the divided beams, which is detected by one of the photodiodes of homodyne detector HD_1. Trace (ii) shows a noise spectrum of a subtraction signal from both photodiodes.

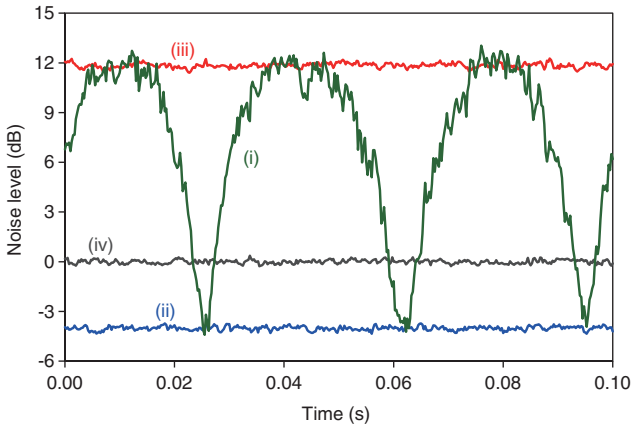

Figure 9: Experimental result of balanced homodyne measurement of squeezed light in the photonic chip. Squeezed light is generated with a pump power of 100 mW. Trace (i): LO phase is scanned. Trace (ii): LO phase is locked at the squeezed quadrature. Trace (iii): LO phase is locked at the anti-squeezed quadrature. Trace (iv): the shot noise level is normalized to 0 dB. Traces (ii), (iii), and (iv) are averaged 20 times. The measurement is performed at the 1.5 MHz side band of the laser frequency in order to avoid a noise from stray light [24].

power for OPO_1 is 100 mW. The resolution bandwidth is 30 kHz, and the video bandwidth is 300 Hz. The measurement is performed at the 1.5 MHz side band of the laser frequency in order to avoid a noise from stray light. Trace (iv) is a shot noise level normalized to 0 dB with only the local oscillator LO_1 injecting to balanced homodyne detector HD_1. Therefore, it corresponds to a vacuum noise level amplified by the local oscillator amplitude. Trace (i) is a noise level observed while the local oscillator phase is scanned by using a piezo-electric controller. The observed signal varied between a squeezed and anti-squeezed noise level. Such a phase-sensitive noise is a characteristic property of squeezed light. Traces (ii) and (iii) are noise levels, while the local oscillator phase is locked at the squeezed and anti-squeezed quadrature, respectively. The observed noise levels are -4.02±0.13 dB for squeezing and +11.85±0.15 dB for anti-squeezing, respectively.

The measurement was repeated at different pump powers. The squeezing and anti-squeezing levels as the pump power is varied are summarized in Figure 10 [24] and indicated by blue circles and red squares, respectively. The normalized pump parameter x is defined as $\sqrt{P/P_{th}}$, where P mW is a pump power and P_{th}=179 mW is the oscillation threshold power, which is obtained by measurement of the classical parametric amplification for the OPO_1. The solid curves in Figure 10 show the calculation results based on the theoretical formula described in Section 3.5, and agree well with the experimental results.

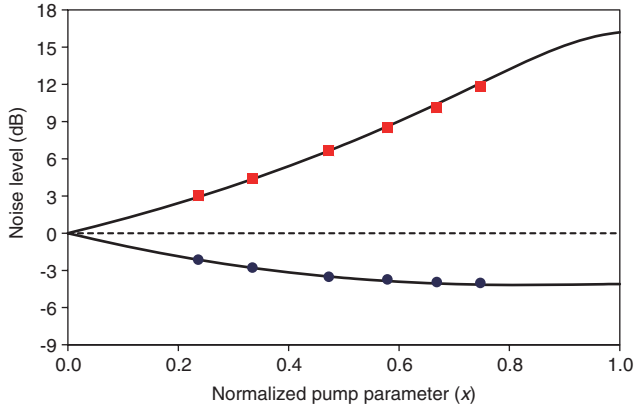

Figure 10: Pump power dependence of squeezing and anti-squeezing levels. Circles and squares indicate observed squeezing and anti-squeezing levels, respectively. Solid curves show the results of numerical calculations with almost perfect mode-matching efficiency (=0.995) between squeezed light and local oscillator [24].

The saturation of the squeezing level at around -4 dB, corresponding to about 0.2 of an average photon number, at a higher pump power is predominantly caused by an insufficient overall coupling efficiency η_c (=0.72) described in Section 3.2. If perfect coupling efficiency is assumed, -8.4 dB of the squeezing level is expected. Another important factor for efficient homodyne detection is visibility η_V, which is a degree of mode matching between squeezed light SL_1 and local oscillator LO_1 in beam splitter BS_2. In these calculations, visibility η_V is set at 0.995. The agreement between the experimental values and calculations verify a high degree of mode-matching efficiency. Almost perfect visibility (0.995) is also achieved by direct measurement of an interference signal between two coherent beams using beam splitter BS_2.

As a result, the waveguide beam splitter makes it possible to achieve an exact 50/50 splitting ratio by tuning the current of the phase shifter and a high degree of mode matching (0.995), and then to realize efficient balanced homodyne measurement. By using the side-band measurement, it is also possible to avoid the harmful effects of stray light and to detect high levels of squeezing. These results demonstrate the high performances of an integrated device for balanced homodyne measurement, which is necessary for CV operations.

3.5 Theoretical formula for squeezing and anti-squeezing levels

In this section, a theoretical formula is provided for the on-chip balanced homodyne measurement of squeezed light. The solid curves in Figure 10 represent the theoretical values of noise levels at various values of the normalized pump parameter x. The noise spectrum $R_\pm$ for the anti-squeezed (+) and squeezed (-) quadrature can be written as [27, 28]

$$R_\pm = 1 \pm \rho\eta \frac{4x}{(1\mp x)^2 + 4f^2}, \tag{4}$$

where f is a measurement frequency normalized by an optical cavity line width, ρ is escape efficiency, and η is homodyne detection efficiency. In this experiment, a cavity line width is estimated as 11.8 MHz and a measurement frequency at side-band mode is 1.5 MHz. Then, normalized measurement frequency f is obtained as 0.127. Homodyne detection efficiency η is described as $\eta = \eta_{PD} * \eta_P * \eta_C * \eta_V^2$. η_{PD} (=0.998) is the quantum efficiency of photodiodes used in the homodyne detector. η_P (=0.99) is the propagation efficiency of an optical path in a free space between the OPO_1 output coupler and the fiber coupling lens. η_C (=0.72) is the overall coupling efficiency as described in Section 3.2. η_V (=0.995) is the visibility between the OPO_1 output mode and local oscillator LO_1 at beam splitter BS_2, as described in Section 3.4. These values yield homodyne detection efficiency η of 0.704.

Escape efficiency ρ is expressed as $T=T/(T+L)$, where T (=0.113) is transmissivity and L is intracavity loss of OPO_1. In PPKTP crystals, it is reported that an intracavity loss L increases with pump beam power at 430 nm [41]. This phenomenon is called as blue-light-induced infrared absorption (BLIIRA). If BLIIRA exists, an intracavity loss is modeled as a function of pump power P and expressed as $L=L_0+aP$, where L_0 is a passive loss without a pump beam and a is a coefficient for pump-induced losses. The pump-induced loss is precisely measured in a PPKTP crystal. L_0 and a are evaluated as 0.00254 and a=0.00922 (W^{-1}), respectively. These results yield escape efficiency ρ at around 0.97.

In order to evaluate precise values for the squeezed and anti-squeezed spectra, it is necessary to consider another experimental imperfection. In actual homodyne measurement, phase fluctuation $\delta\theta$ between squeezed light and local oscillator, which is caused by the imperfection of phase locking, degrades the observed squeezing and anti-squeezing levels. The noise levels given by Eq. (4) are modified as

$$R'_\pm = R_\pm \cos^2\delta\theta + R_\mp \sin^2\delta\theta, \tag{5}$$

due to the effect of phase fluctuation $\delta\theta$ [43]. In the optical configuration here, phase fluctuation $\delta\theta$ is estimated as 1.5°. It is also necessary to consider the effect of an

electrical circuit noise of homodyne detection. If clearance C of the shot noise level above the electrical circuit noise is taken into account, the final noise spectra are obtained as

$$R''_{\pm}=R'_{\pm}\left(1-10^{-\frac{C}{10}}\right)+10^{-\frac{C}{10}}. \quad (6)$$

The clearance C is evaluated as 13.5 dB with the local oscillator power of 3.5 mW. By using the experimental parameters described above, the theoretical values of noise levels are calculated as shown by solid lines in Figure 10. The results agree well with the experimental values.

4 EPR beams in a photonic chip

4.1 Heisenberg representation of EPR beams and inseparability criterion

This section reviews the generation of EPR beams and the verification of quantum entanglement in a photonic chip. EPR beams are generated by combining two squeezed light beams with a 50/50 beam splitter. In this process, the relative optical phase φ between two squeezed light beams is an important experimental parameter. Here, we schematically show typical cases with different values of φ in phase space representation. When φ is 90°, the final outputs seem to be phase-insensitive noises as shown in Figure 11A. However, there is quantum entanglement between quadrature phase amplitude of outputs EPR_1 and EPR_2. On the other hand, when φ is 0°, the outputs are two-independent squeezed light SL_1' and SL_2', as shown in Figure 11B, and there is no quantum correlation between them.

The theoretical expression for the above explanations is presented here by using the Heisenberg representation with the optical configuration of Figure 12. Firstly, two single-mode squeezed light beams, SL_1 and SL_2, are obtained by using two-independent squeezers that act on vacuum states Vac_1 and Vac_2, and are described as squeezing operators $S(r)$ and $S(-r)$ with squeezing parameter r, respectively. The phase shifter gives the optical phase shift φ to the squeezed light SL_2. The quadrature phase amplitude operators $\hat{x}_i^{(0)}$ and $\hat{p}_i^{(0)}$ of the initial vacuum state Vac_i (i=1, 2) are introduced. They correspond to cosine and sine components of the optical field. Then, the complex amplitude operators of squeezed light beams SL_1 and SL_2 can be written as

$$\hat{a}_1=e^{-r}\hat{x}_1^{(0)}+ie^{r}\hat{p}_2^{(0)}, \quad (7)$$

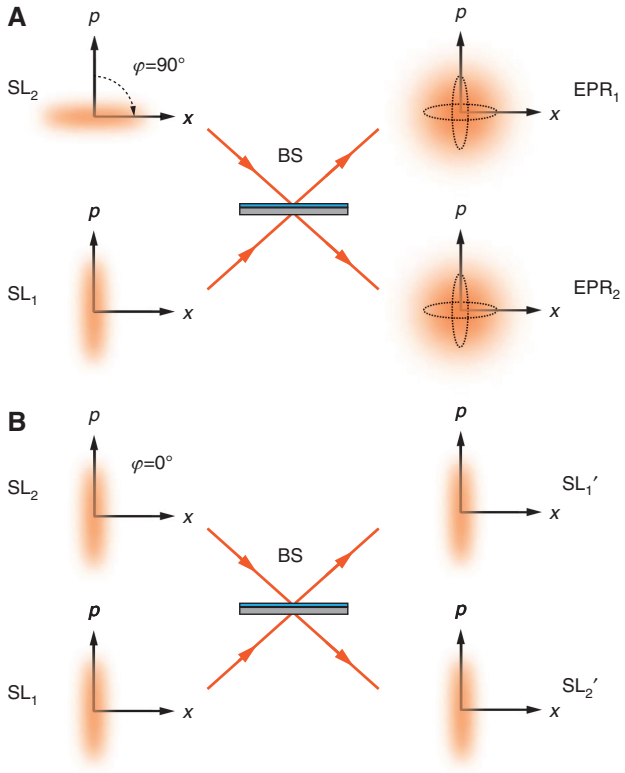

Figure 11: Phase space representation of two outputs. (A) Outputs are entangled EPR_1 and EPR_2 beams when the incident squeezed light beams SL_1 and SL_2 are combined with relative phase φ of 90°. (B) Outputs are two independent squeezed light SL_1' and SL_2' when the squeezed light beams SL_1 and SL_2 are combined with φ of 0°.

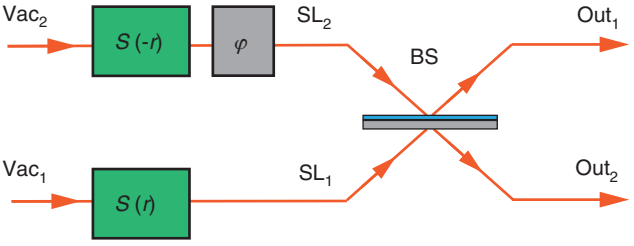

Figure 12: Optical model for generating entangled EPR beams. The incident single-mode squeezed light beams SL_1 and SL_2 are generated by using squeezers $S(r)$ and $S(-r)$, which operate on vacuum states Vac_1 and Vac_2, respectively, and are characterized by the same squeezing parameter r. Squeezed light SL_2 passes through a phase shifter, which produces phase shift φ and is combined with squeezed light SL_1 at 50/50 beam splitter BS. The final output states Out1 and Out2 vary depending on the value of φ.

$$\hat{a}_2=e^{i\varphi}(e^{-r}\hat{x}_2^{(0)}+ie^{r}\hat{p}_2^{(0)}). \quad (8)$$

It is assumed that two squeezers are characterized by the same squeezing parameter r, and both squeezed light beams SL_1 and SL_2 are pure states. The squeezed light

beams SL_1 and SL_2 are combined using 50/50 beam splitter BS. Then, the complex amplitude operators of outputs Out_1 and Out_2 are derived as

$$\begin{aligned}\hat{A}&=\hat{x}_1+i\hat{p}_1\\&=\frac{1}{\sqrt{2}}(e^{-r}\hat{x}_1^{(0)}+\cos\varphi e^{-r}\hat{x}_2^{(0)}-\sin\varphi e^{r}p_2^{(0)})+\\&\frac{i}{\sqrt{2}}(e^{r}\hat{p}_1^{(0)}+\sin\varphi e^{-r}\hat{x}_2^{(0)}+\cos\varphi e^{r}\hat{p}_2^{(0)}\end{aligned} \tag{9}$$

$$\begin{aligned}\hat{A}&=\hat{x}_2+i\hat{p}_2\\&=\frac{1}{\sqrt{2}}(-e^{-r}\hat{x}_1^{(0)}+\cos\varphi e^{-r}\hat{x}_2^{(0)}-\sin\varphi e^{r}p_2^{(0)})+\\&\frac{i}{\sqrt{2}}(-e^{r}\hat{p}_1^{(0)}+\sin\varphi e^{-r}\hat{x}_2^{(0)}+\cos\varphi e^{r}p_2^{(0)}),\end{aligned} \tag{10}$$

where the $\hat{x}_i$ and $\hat{p}_i$ are quadrature phase amplitude operators of output Out_i (i=1, 2). The variances of x and p quadratures from output Out_i are calculated as

$$\langle\Delta\hat{x}_i^2\rangle=\frac{1}{4}\left(\frac{1+\cos^2\varphi}{2}e^{-2r}+\frac{1}{2}\sin^2\varphi e^{2r}\right), \tag{11}$$

$$\langle\Delta\hat{p}_i^2\rangle=\frac{1}{4}\left(\frac{1}{2}\sin^2\varphi e^{-2r}+\frac{1+\cos^2\varphi}{2}e^{2r}\right) \tag{12}$$

using a relation of $\langle\Delta\hat{x}_i^{(0)^2}\rangle=\langle\Delta\hat{p}_i^{(0)^2}\rangle=\frac{1}{4}\left(\hbar=\frac{1}{2}\right)$, which corresponds to a noise variance in a vacuum state.

To verify quantum correlation in final outputs, an inseparability criterion is necessary. For that purpose, it is required to introduce correlation variance in quadrature phase amplitudes between two outputs Out_1 and Out_2 as

$$\Delta_{1,2}^2=\langle[\Delta(\hat{x}_1-\hat{x}_2)]^2\rangle+\langle[\Delta(\hat{p}_1+\hat{p}_2)]^2\rangle. \tag{13}$$

It has been proven by Duan et al. [44] and Simon [45] that the two outputs Out_1 and Out_2 are inseparable and show quantum entanglement when

$$\Delta_{1,2}^2<1. \tag{14}$$

Equation (14) gives the sufficient condition for quantum entanglement and is often used as the inseparability criterion. In the optical configuration of Figure 12, the correlation variance is derived as

$$\Delta_{1,2}^2=\frac{1}{2}(e^{-2r}+\sin^2\varphi e^{-2r}+\cos^2\varphi e^{2r}). \tag{15}$$

Notice that the value of Eq. (15) is 1 when the squeezing parameter r is zero. It means that the outputs are actually two independent vacuum states, so there is no quantum correlation between them.

When φ is 90°, the variances of x_i and p_i quadrature of output Out_i (i=1, 2) are given as

$$\langle\Delta\hat{x}_i^2\rangle=\langle\Delta\hat{p}_i^2\rangle=\frac{1}{4}\left(\frac{1}{2}e^{-2r}+\frac{1}{2}e^{2r}\right). \tag{16}$$

The correlation variance is calculated as

$$\Delta_{1,2}^2=e^{-2r}. \tag{17}$$

The final outputs are entangled EPR_1 and EPR_2 beams, as the correlation variance satisfies the inseparability criterion $\Delta_{1,2}^2<1$ as long as squeezing parameter r is larger than zero. They show a phase-insensitive noise as x and p quadratures have the same noise variances as shown by Eq. (16) and in Figure 11A schematically. Notice that the value of $\Delta_{1,2}^2$ goes to zero in the ideal case with an infinite amount of squeezing parameter r, achieving perfect correlation. On the other hand, when φ is 0°, the variances of x_i and p_i quadrature of output Out_i (i=1, 2) are given as

$$\langle\Delta\hat{x}_i^2\rangle=\frac{1}{4}e^{-2r}, \tag{18}$$

$$\langle\Delta\hat{p}_i^2\rangle=\frac{1}{4}e^{2r}. \tag{19}$$

The correlation variance is calculated as

$$\Delta_{1,2}^2=\frac{1}{2}(e^{-2r}+e^{2r}). \tag{20}$$

The final outputs are two independent squeezed light SL_1' and SL_2' and show phase-sensitive noise as shown by Eqs. (18) and (19) and in Figure 11B schematically. It can be easily seen that $\Delta_{1,2}^2$ breaks the inseparability criterion and then there is no quantum correlation between outputs.

4.2 Experimental setup

Figure 13 [24] shows the experimental setup for generating and characterizing EPR beams utilizing four variable beam splitters integrated in a photonic chip. Beam splitters BS_1, BS_2, and BS_4 are tuned at a 50/50 beam-splitting ratio, and BS_3 is tuned at 99/1. To guide the output from one beam splitter to another, two fibers are connected mechanically using mating sleeves designed for FC/APC. The additional squeezed light SL_2 is generated by extra optical parametric oscillator OPO_2 outside the chip, which has the same optical configuration with OPO_1. Firstly, two squeezed light beams SL_1 and SL_2 are combined at beam splitter BS_2. At the same time, weak coherent beams are introduced

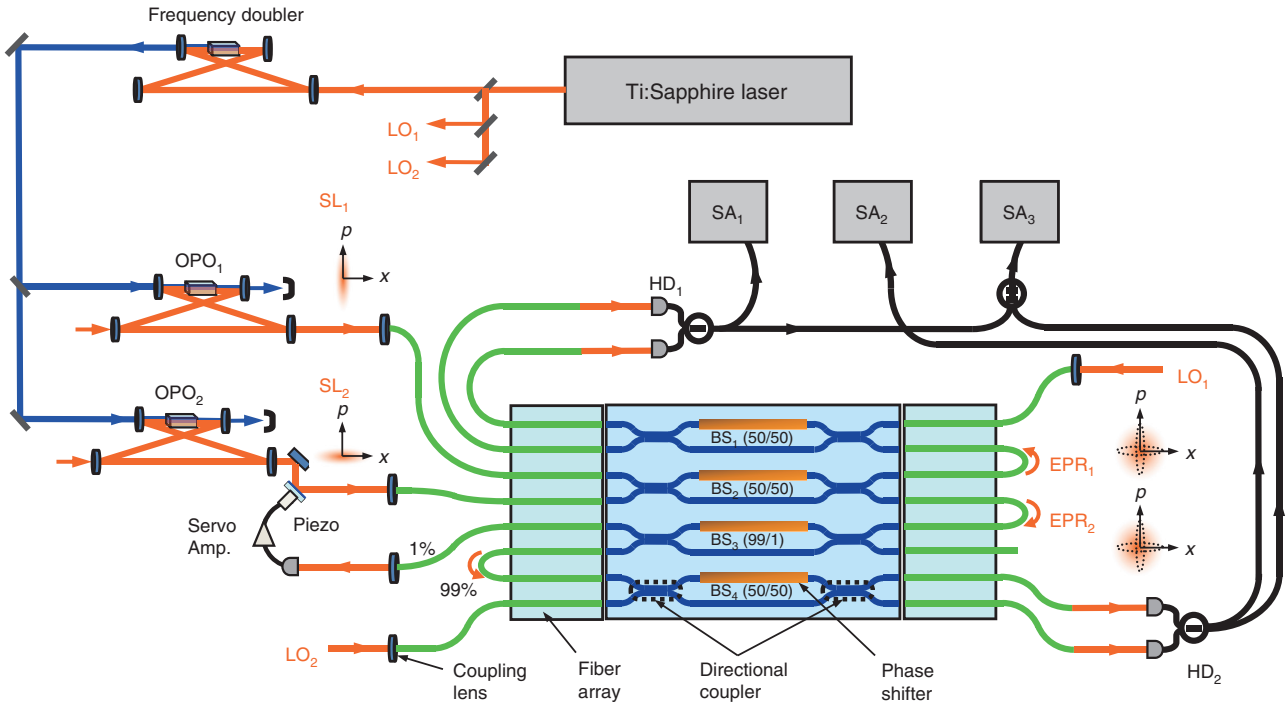

Figure 13: Experimental setup for the generation and verification of entangled EPR beams in the photonic chip where four variable beam splitters are integrated. Continuous-wave squeezed light beams SL_1 and SL_2 (at 860 nm) are generated by subthreshold optical parametric oscillators OPO_1 and OPO_2 outside the chip. Two squeezed light beams SL_1 and SL_2 are firstly combined at 50/50 beam splitter BS_2. Weak coherent beams are introduced into both OPOs. One percent of interference signals between them is picked up by 99/1 beam splitter BS_3 and used for phase locking between squeezed light beams SL_1 and SL_2 at 90° using a servo-amplifier and piezo-actuator. Output beam EPR_1 (EPR_2) is combined with local oscillator LO_1 (LO_2) at 50/50 beam splitter BS_1 (BS_4) and then detected by balanced homodyne detector HD_1 (HD_2) [24].

into both OPOs for the purpose of phase locking. One percent of the interference signals from those beams is picked up by beam splitter BS_3. Then, this signal is used for phase locking the relative phase φ between squeezed light beams SL_1 and SL_2 at 90° using a servo-amplifier and piezo-actuator. By this means, the entangled beams EPR_1 and EPR_2 are generated within the photonic chip. The output beam EPR_1 (EPR_2) is combined with local oscillator LO_1 (LO_2) at beam splitter BS_1 (BS_4). Then, the noise levels for both quadratures $\langle\Delta\hat{x}_1^2\rangle$ ($\langle\Delta\hat{x}_2^2\rangle$) and $\langle\Delta\hat{p}_1^2\rangle$ ($\langle\Delta\hat{p}_2^2\rangle$) of the output EPR_1 (EPR_2) beam are detected by balanced homodyne detector HD_1 (HD_2). Finally, the variance of difference signals $\langle[\Delta(\hat{x}_1\text{-}\hat{x}_2)]^2\rangle$ and sum signals $\langle[\Delta(\hat{p}_1+\hat{p}_2)]^2\rangle$ are measured using a hybrid junction to check the inseparability criterion.

4.3 Generation and verification of EPR beams

Figure 14A and B [24] show the noise levels of output beams as the phases of local oscillator LO_1 and LO_2 are varied, respectively. The experiment is performed at the 1.5 MHz side band of the laser frequency. The setting of spectrum analyzer is same as the experiments shown in Figures 9 and 10. Trace (i) represents the noise of one of the output beams as relative phase φ between incident squeezed light beams SL_1 and SL_2 is varied while simultaneously scanning the LO phase on a faster timescale. So, the output seems to continuously vary depending on φ [46]. At the moment that φ is 0°, which is indicated by dashed arrows, the outputs are two independent squeezed light beams. The noise levels periodically change from anti-squeezed to squeezed quadrature depending on the LO phase. On the other hand, at the moment that φ is 90°, which is indicated by solid arrows, the outputs are the entangled EPR_1 and EPR_2 beams. Traces (ii) and (iii) represent the noise levels of the x and p quadratures when φ is locked at 90°. The output EPR_1 beam shows the noise levels of $\langle\Delta\hat{x}_1^2\rangle$=+4.91±0.13 dB and $\langle\Delta\hat{p}_1^2\rangle$=+4.85±0.15 dB at homodyne detector HD_1. Moreover, the output EPR_2 shows the noise levels of $\langle\Delta\hat{x}_2^2\rangle$=+4.10±0.12 dB and $\langle\Delta\hat{p}_2^2\rangle$=+4.18±0.13 at homodyne detector HD_2 above the shot noise level without incident squeezed light beams

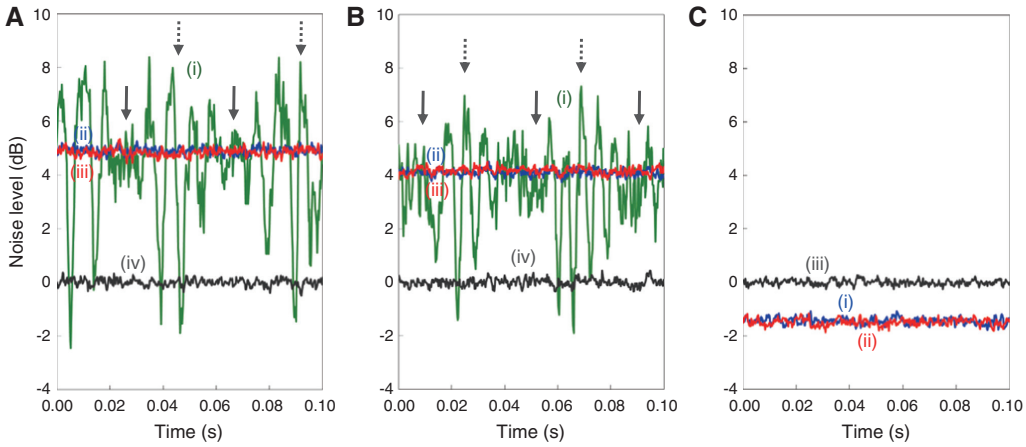

Figure 14: Generation of EPR beams and verification of quantum entanglement. (A) Noise levels of output EPR_1 beam. (B) Noise levels of output EPR_2 beam. Trace (i): noise levels as the relative phase φ between incident squeezed light beams SL_1 and SL_2 is changed and the LO phase is simultaneously scanned with a faster timescale. Traces (ii) and (iii): noise levels where the LO phase is locked at the x and p quadratures with the φ locked at 90°. Trace (iv): shot noise level normalized to 0 dB. (C) Measurement to check the inseparability condition. Traces (i) and (ii) represent $\langle[\Delta(\hat{x}_1\text{-}\hat{x}_2)]^2\rangle$ and $\langle[\Delta(\hat{p}_1+\hat{p}_2)]^2\rangle$, respectively, and trace (iii) shows the noise level without quantum correlation [24].

represented by trace (iv). This phase-insensitive behavior is one of the essential properties of EPR beams.

Finally, $\langle[\Delta(\hat{x}_1\text{-}\hat{x}_2)]^2\rangle$ and $\langle[\Delta(\hat{p}_1+\hat{p}_2)]^2\rangle$ are measured to check the inseparability criterion. Trace (i) in Figure 14C shows the variance of the difference signal between $\hat{x}_1$ from HD_1 and $\hat{x}_2$ and from HD_2. Trace (ii) represents the variance of the sum signal between $\hat{p}_1$ and $\hat{p}_2$ obtained in the same way. The measurement shows $\langle[\Delta(\hat{x}_1\text{-}\hat{x}_2)]^2\rangle$=-1.44±0.12 dB and $\langle[\Delta(\hat{p}_1+\hat{p}_2)]^2\rangle$=-1.49±0.12 dB below the noise level without quantum correlation, as shown by trace (iii). These results yield a correlation variance of $\Delta^2_{1,2}$=0.71 and satisfy the inseparability criterion, proving the generation of EPR beams and verification of quantum entanglement within the photonic chip. This is because of the attainment of almost perfect mode matching between two light beams in waveguide beam splitters. In addition, the utilization of the side band makes it possible to simultaneously introduce both non-classical light and highly intense coherent beam to a chip and achieve highly efficient balanced homodyne measurement without noises around the laser frequency caused by stray light. So, the utilization of side bands in CV experiments could be the best solution for the optical integration. In the present experiment, a single chip is used; however, different interferometers are concatenated using optical fibers. Coupling in and out of the chip is the major contributor to loss and then limits the total amount of entanglement. This can be dramatically reduced by concatenating circuits in a monolithic chip [34, 35].

5 Conclusion and outlook

Entanglement is an essentially important resource for the majority of quantum information science and technologies. In this article, we reviewed the currently developed scheme for generating quantum entanglement using integrated waveguide circuits. As an example of DV entanglement, the experiment for generating a photon-entangled state was reviewed. As an example of CV entanglement, we reviewed the current study of generation of EPR beams. It also includes balanced homodyne measurement as a method to detect a quantum state of light and verify the inseparability in CV entangled states. The use of high-quality interference due to the almost perfect mode matching in waveguide circuits and side bands of the optical field to avoid the noise caused by stray light enables simultaneous operation on non-classical light and intense coherent beams in a single photonic chip. The demonstration of all the key components for Gaussian operations within a photonic chip, including the generation and characterization of EPR beams and the verification of entanglement, points the way to full optical integration of CV and hybrid quantum information processing.

For a future outlook, integrated squeezing and non-Gaussian operations like photon counting are required to realize universal quantum information processing [47]. Generation of single-mode squeezed light is demonstrated by using a waveguide device consisting of a non-linear optical crystal such as $LiNbO_3$ [48–50] or $KTiOPO_4$ [51, 52].

Generation of CV entanglement is also demonstrated by mixing two single-mode squeezed light beams generated by two $LiNbO_3$ waveguides with a bulk beam splitter [53]. Recent theoretical work proposes the possibility of full optical integration for generating CV entanglement using non-linear waveguide arrays [54]. Another approach to achieve integrated squeezing is to use an on-chip micro-resonator such as a silicon micromechanical resonator [55] or a silicon nitride microring resonator that utilizes a four-wave mixing process [56]. Integrated semiconductor detectors [57] or superconducting single-photon detectors [58, 59] are promising and will enable the use of side-band techniques using a recently developed optical high-pass filter [60], thereby eliminating the influence of stray light that would affect the dark counts. These results will yield the way to universal quantum information processing within a monolithic photonic chip.

References

[1] Bennett CH, Brassard G, Crépeau C, Jozsa R, Peres A, Wootters WK. Teleporting an unknown quantum state via dual classical and Einstein-Podolsky-Rosen channels. Phys Rev Lett 1993;70:1895–9.

[2] Bouwmeester D, Pan JW, Mattle K, Eibl M, Weinfurter H, Zeilinger A. Experimental quantum teleportation. Nature 1997;390:575–9.

[3] Furusawa A, Sørensen JL, Braunstein SL, Fuchs CA, Kimble HJ, Polzik ES. Unconditional quantum teleportation. Science 1998;282:706–9.

[4] O'Brien JL. Optical quantum computing. Science 2007;318:1567–70.

[5] Weedbrook C, Pirandola S, García-Patrón R, Cerf NJ, Ralph TC, Shapiro JH, Lloyd S. Gaussian quantum information. Rev Mod Phys 2012;84:621–69.

[6] Kwait PG, Mattle K, Weinfurter H, Zeilinger A, Sergienko AV, Shih Y. New high-intensity source of polarization-entangled photon pairs. Phys Rev Lett 1995;75:4337–41.

[7] Lee H, Kok P, Dowling JP. A quantum Rosetta stone for interferometry. J Mod Opt 2002;49:2325–38.

[8] Einstein A, Podolsky B, Rosen N. Can quantum-mechanical description of physical reality be considered complete? Phys Rev 1935;47:777–80.

[9] Furusawa A, van Loock P. Quantum teleportation and entanglement: a hybrid approach to optical quantum information processing. Verlag: Wiley-VCH, 2011.

[10] Takeda S, Mizuta T, Fuwa M, van Loock P, Furusawa A. Deterministic quantum teleportation of photonic quantum bits by a hybrid technique. Nature 2013;500:315–8.

[11] Raussendorf R, Briegel HJ. A one-way quantum computer. Phys Rev Lett 2001;86:5188–91.

[12] Menicucci NC, van Loock P, Gu M, Weedbrook C, Ralph TC, Nielsen MA. Universal quantum computation with continuous-variable cluster states. Phys Rev Lett 2006;97:110501.

[13] van Loock P, Weedbrook C, Gu M. Building Gaussian cluster states by linear optics. Phys Rev A 2007;76:032321.

[14] Menicucci NC, Flammia ST, Pfister O. One-way quantum computing in the optical frequency comb. Phys Rev Lett 2008;101:130501.

[15] Yukawa M, Ukai R, van Loock P, Furusawa A. Experimental generation of four-mode continuous-variable cluster states. Phys Rev A 2008;78:012301.

[16] Ukai R, Iwata N, Shimokawa Y, Armstrong SC, Politi A, Yoshikawa J, van Loock P, Furusawa A. Demonstration of unconditional one-way quantum computations for continuous-variables. Phys Rev Lett 2011;106:240504.

[17] Yokoyama S, Ukai R, Armstrong SC, Sornphiphatphong C, Kaji T, Suzuki S, Yoshikawa J, Yonezawa H, Menicucci NC, Furusawa A. Ultra-large-scale continuous-variable cluster states multiplexed in the time domain. Nat Photon 2013;7:982–6.

[18] Menicucci NC. Fault-tolerant measurement-based quantum computing with continuous-variable cluster state. Phys Rev Lett 2014;112:120504.

[19] Gottesman D, Kitaev A, Preskill J. Encoding a qubit in an oscillator. Phys Rev A 2001;64:012310.

[20] Vasconcelos HM, Sanz L, Glancy S. All-optical generation of states for "Encoding a qubit in an oscillator." Opt Lett 2010;35:3261–3.

[21] Politi A, Cryan MJ, Rarity JG, Yu S, O'Brien JL. Silica-on-silicon waveguide quantum circuits. Science 2008;320:646–9.

[22] Matthews JCF, Politi A, Stefanov A, O'Brien JL. Manipulation of multiphoton entanglement in waveguide quantum circuits. Nat Photon 2009;3:346–50.

[23] Laing A, Peruzzo A, Politi A, Verde MR, Halder M, Ralph TC, Thompson MG, O'Brien JL. High-fidelity operation of quantum photonic circuits. Appl Phys Lett 2010;97:211109.

[24] Masada G, Miyata K, Politi A, Hashimoto T, O'Brien JL, Furusawa A. Continuous-variable entanglement on a chip. Nat Photon 2015;9:316–9.

[25] Khan I, Wittmann C, Jain N, Killoran N, Lütkenhaus N, Marquardt C, Leuchs G. Optimal working points for continuous-variable quantum channels. Phys Rev A 2013;88:010302.

[26] Wittmann C, Fürst J, Wiechers C, Elser D, Häseler H, Lütkenhaus N, Leuchs G. Witnessing effective entanglement over a 2 km fiber channel. Opt Exp 2010;18:4499–509.

[27] Lorenz S, Rigas J, Heid M, Andersen UL, Lütkenhaus N, Leuchs G. Witnessing effective entanglement in a continuous variable prepare-and-measure setup and application to a quantum key distribution scheme using postselection. Phys Rev A 2006;74:042326.

[28] Jouguet P, Kunz-Jacques P, Leverrier A, Grangier P, Diamanti E. Experimental demonstration of long-distance continuous-variable quantum key distribution. Nat Photon 2013;7:378–81.

[29] Lodewyck J, Bloch M, García-Patrón R, Fossier S, Karpov E, Diamanti E, Debuisschert T, Cerf NJ, Tualle-Brouri R, McLaughlin SW, Grangier P. Quantum key distribution over 25 km with an all-fiber continuous-variable system. Phys Rev A 2007;76:042305.

[30] Hong CK, Ou ZY, Mandel L. Measurement of subpicosecond time intervals between two photons interference. Phys Rev Lett 1987;59:2044–6.

[31] Giovannetti V, Loyd S, Maccone L. Quantum metrology. Phys Rev Lett 2006;96:010401.

[32] Boto AN, Kok P, Abrams DS, Braunstein SL, Williams CP, Dowling JP. Quantum interferometric optical lithography: exploiting entanglement to beat the diffraction limit. Phys Rev Lett 2000;85:2733–6.
[33] Knill E, Laflamme R, Milburn GJ. A scheme for efficient quantum computation with linear optics. Nature 2001;409:46–52.
[34] Carolan J, Harrold C, Sparrow C, Martín-López E, Russell NJ, Silverstone JW, Shadbolt PJ, Matsuda N, Oguma M, Itoh M, Marshall GD, Thompson MG, Matthews JCF, Hashimoto T, O'Brien JL, Laing A. Universal linear optics. Science 2015;349:711–5.
[35] Harris NC, Steinbrecher GR, Mower J, Lahini Y, Prabhu M, Baehr-Jones T, Hochberg M, Lloyd S, Englund D. Bosonic transport simulations in a large-scale programmable nanophotonic processor. arXiv:1507.03406.
[36] Setzpfandt F, Solntsev AS, Titchener J, Wu CW, Xiong C, Schiek R, Pertsch T, Neshev DN, Sukhorukov AA. Tunable generation of entangled photons in a nonlinear directional coupler. Laser Photon Rev 2016;10:131–6.
[37] Solntsev AS, Setzpfandt F, Clark AS, Wu CW, Collins MJ, Xiong C, Schreiber A, Katzschmann F, Eilenberger F, Schiek R, Sohler W, Mitchell A, Silberhorn C, Eggleton BJ, Pertsch T, Sukhorukov AA, Neshev DN, Kivshar YS. Generation of nonclassical biphoton states through cascaded quantum walks on a nonlinear chip. Phys Rev X 2014;4:031007.
[38] Silverstone JW, Bonneau D, Ohira K, Suzuki N, Yoshida H, Iizuka N, Ezaki M, Natarajan CM, Tanner MG, Hadfield RH, Zwiller V, Marshall GD, Rarity JG, O'Brien JL, Thompson MG. On-chip quantum interference between silicon photon-pair sources. Nat Photon 2014;8:104–8.
[39] Yuen HP, Chan VWS. Noise in homodyne and heterodyne detection. Opt Lett 1983;8:177–9.
[40] Suzuki S, Yonezawa H, Kannari F, Sasaki M, Furusawa A. 7 dB quadrature squeezing at 860 nm with periodically poled $KTiOPO_4$. Appl Phys Lett 2006;89:061116.
[41] Takeno Y, Yukawa M, Yonezawa H, Furusawa A. Observation of -9 dB quadrature squeezing with improvement of phase stability in homodyne measurement. Opt Exp 2007;15:4321–7.
[42] Masada G, Suzudo T, Satoh Y, Ishizuki H, Taira T, Furusawa A. Efficient generation of highly squeezed light with periodically poled MgO:$LiNbO_3$. Opt Exp 2010;18:13114–21.
[43] Aoki T, Takahashi G, Furusawa A. Squeezing at 946 nm with periodically-poled $KTiOPO_4$. Opt Exp 2006;14:6930–5.
[44] Duan LM, Giedke G, Cirac JI, Zoller P. Inseparability criterion for continuous variable systems. Phys Rev Lett 2000;84:2722–5.
[45] Simon R. Peres-Horodecki separability criterion for continuous variable systems. Phys Rev Lett 2000;84:2726–9.
[46] Zhang TC, Goh KW, Chou CW, Lodahl P, Kimble HJ. Quantum teleportation of light beams. Phys Rev A 2003;67:033802.
[47] Dakna M, Anhut T, Opatrný T, Knöll L, Welsch DG. Generating Schrödinger-cat-like states by means of conditional measurements on a beam splitter. Phys Rev A 1997;55:3184–94.
[48] Serkland DK, Fejer MM, Byer RL, Yamamoto Y. Squeezing in quasi-phase-matched $LiNbO_3$ waveguide. Opt Lett 1995;20:1649–51.
[49] Kanter GS, Kumar P, Roussev RV, Kurz J, Parameswaran KR, Fejer MM. Squeezing in a LiNbO3 integrated optical waveguide circuit. Opt Exp 2002;10:177–82.
[50] Eto Y, Koshino A, Ohshiro A, Sakurai J, Horie K, Hirano T, Sasaki M. Efficient homodyne measurement of picosecond squeezed pulses with pulse shaping technique. Opt Lett 2011;36:4653–5.
[51] Anderson ME, Beck M, Raymer MG, Bierlein JD. Quadrature squeezing with ultrashort pulses in nonlinear-optical waveguides. Opt Lett 1995;20:620–2.
[52] Pysher M, Bloomer R, Pfister O, Kaleva CM, Roberts TD, Battle P. Broadband amplitude squeezing in a periodically poled $KTiOPO_4$ waveguide. Opt Lett 2009;34:256–8.
[53] Yoshino K, Aoki T, Furusawa A. Generation of continuous-wave broadband entangled beams using periodically poled lithium niobate waveguides. Appl Phys Lett 2007;90:041111.
[54] Rai A, Angelakis DG. Dynamics of nonclassical light in integrated nonlinear waveguide arrays and generation of robust continuous-variable entanglement. Phys Rev A 2012;85:052330.
[55] Safavi-Naeini AH, Gröblacher S, Hill JT, Chan J, Aspelmeyer M, Painter O. Squeezed light from a silicon micromechanical resonator. Nature 2013;500:185–9.
[56] Dutt A, Luke K, Manipatruni S, Gaeta AL, Nussenzveig P, Lipson M. On-chip optical squeezing. Phys Rev Appl 2015;3:044005.
[57] Campbell JC. Recent advances in telecommunications avalanche photodiodes. J Lightw Technol 2007;25:109–21.
[58] Sprengers JP, Gaggero A, Sahin D, Jahanmirinejad S, Frucci G, Mattioli F, Leoni R, Beetz J, Lermer M, Kamp M, Höfling S, Sanjines R, Fiore A. Waveguide superconducting single-photon detectors for integrated quantum photonic circuits. Appl Phys Lett 2011;99:181110.
[59] Pernice WHP, Schuck C, Minaeva O, Li M, Goltsman GN, Sergienko AV, Tang HX. High-speed and high-efficiency travelling wave single-photon detectors embedded in nanophotonic circuits. Nat Commun 2012;3:1325.
[60] Takeda S, Benichi H, Mizuta T, Lee N, Yoshikawa J, Furusawa A. Quantum mode filtering of non-Gaussian states for teleportation-based quantum information processing. Phys Rev A 2012;85:053824.

Graphical abstract

Genta Masada and Akira Furusawa

On-chip continuous-variable quantum entanglement

DOI 10.1515/nanoph-2015-0142
Nanophotonics 2016; x: xxx–xxx

Review article: We review the currently developed method for generation and verification of continuous-variable quantum entanglement using a photonic chip where waveguide circuits are integrated.

Keywords: silica-on-silicon chip; waveguide interferometer; EPR beams; squeezed light; balanced homodyne measurement.